The Interaction between Deep Convection and Easterly Wave Activity over Africa: Convective Transitions and Mechanisms

ADEME MEKONNEN

Energy and Environmental Systems Department, North Carolina A&T State University, Greensboro, North Carolina

WILLIAM B. ROSSOW

Cooperative Remote Sensing Science and Technology Institute, City College of New York, New York, New York

ABSTRACT

Recent work using observational data from the International Satellite Cloud Climatology Project (ISCCP) and reanalysis products suggests that African easterly waves (AEWs) form in association with a "transition" process from smaller and scattered convection into larger and organized mesoscale convective activity. However, the transition process is unclear and how mesoscale convection initiates AEWs is not well understood. Analysis based on 25 years of ISCCP and reanalysis datasets show that increasing intradiurnal activity, atmospheric instability, and specific humidity precede the development of well-organized convection over the Ethiopian highlands. Atmospheric instability favors a high frequency of scattered, isolated convection to the east of the Ethiopian highlands, first, followed by a continuing and large increase in instability and increasing humidity, which supports well-organized larger-scale convection. The timing of the changes of thermodynamic variables shows that the dominant transition process is scattered, with weakly organized convection transitioning into the well-organized mesoscale convection, and this initiates the AEWs. Slightly before the mesoscale convection peaks over the Ethiopian highlands, low-level moist westerlies, low- to midlevel wind shear, and positive relative vorticity increase over the region. Evidence shows that the large-scale and local environment enables the scattered and less well-organized convection to merge and form larger and well-organized convection. The dynamic processes suggest that the dominant pathway for AEW initiation is scattered convection transitioning to large and well-organized convection over the Ethiopian highlands and this initiates AEWs westward of the Ethiopian highlands.

1. Introduction

The shorter time scale (<10 day) summer rainfall variability over North Africa is mainly associated with mesoscale convective systems (MCSs; e.g., Hodges and Thorncroft 1997; Mathon and Lauren 2001) and African easterly waves (AEWs; e.g., Reed et al. 1977; Diedhiou et al. 1999). AEWs are also associated with tropical cyclogenesis over the Atlantic (e.g., Avila and Pasch 1992; Russell et al. 2017).

The AEWs are important weather systems whose initiation, variability, and effect on convection, remains an active area of research. The study of AEWs has a long history, going back to the 1950s (e.g., Riehl 1954), 1960s (e.g., Simpson et al. 1968), and 1970s (e.g., Frank 1970; Burpee 1972; Reed et al. 1977). Several theories have been suggested to describe AEW initiation. Burpee (1972) and subsequent studies viewed AEW initiation as related to the presence of an unstable midtropospheric easterly jet in tropical North Africa (e.g., Reed et al. 1977; Albignat and Reed 1980; Norquist et al. 1977; Thorncroft and Hoskins 1994). In contrast, recent studies have argued that the midlevel jet is only marginally unstable (e.g., Hall et al. 2006; Thorncroft et al. 2008), so its presence is not a necessary condition for AEW initiation (e.g., Hsieh and Cook 2005, 2007). Some studies have suggested that AEWs are initiated in association with preexisting convection over East Africa (Fig. 1; e.g., Carlson 1969; Berry and Thorncroft 2005; Lin et al. 2005; Mekonnen et al. 2006; Kiladis et al. 2006). Thorncroft et al. (2008) prescribed a diabatic forcing

at a location just to the west of the Darfur Mountains (Fig. 1) in an idealized numerical model and demonstrated the emergence of wave disturbances as a result of this convective outburst. However, the process by which the mesoscale convection initiates AEWs is less clear.

Diaz and Aiyyer (2013) argued that new AEWs are initiated by energy dispersion from upstream wave packets. Drawing an analogy with downstream development of midlatitude baroclinic eddies, they showed that development of new AEWs is consistent with the direction of ageostrophic geopotential fluxes. They noted that, earlier in their life cycle, AEWs grow via geopotential flux convergence, but further growth occurs through barotropic and baroclinic energy conversions. This, however, does not answer the question as to how the waves are initiated when energy dispersion is nonexistent. This implies that the origin and initiation mechanisms of AEWs are not well understood.

Several studies investigated the case of an AEW that was associated with Hurricane Alberto in the summer of 2000. Berry and Thorncroft (2005) suggested that the pre-Alberto AEW formed to the west of the Darfur Mountains (Fig. 1) in association with large-scale convection over the region on 30 July. Lin et al. (2005) suggested that the same AEW formed in association with topographically generated mesoscale convective activity near the Ethiopian highlands on 28 July. Ventrice and Thorncroft (2013) suggested that the wave formed in association with deep convection triggered by a convectively coupled Kelvin wave on 29–30 July. In contrast, Diaz and Aiyyer (2013) suggested that this AEW was formed as a result of energy dispersion from an old AEW near Ethiopian highlands on 26 July. Overall, different areas of initiation and dissimilar mechanisms were suggested for pre-Alberto AEW.

Using Weather State (WS) data from the International Satellite Cloud Climatology Project (ISCCP) and reanalysis products, Mekonnen and Rossow (2011, hereafter MR11) suggested that stronger latent heating and negative radiative cooling over eastern Africa are associated with larger and better organized convective clouds than weaker and scattered convective clouds. They suggested that less organized convective clouds [referred to as weather state type 3 (WS3) described in section 2a] that originate over the Arabian Sea/northern Indian Ocean region produce a chain of events that lead to better organized mesoscale scale convective systems [referred to as weather state 1 type (WS1) described in section 2a], just to the west of the Ethiopian highlands. It appears that the scattered and less-organized convective systems interact with the Ethiopian highlands and then "transition" to MCS-type cloud regimes and, almost at the same time, easterly wave perturbations emerge west
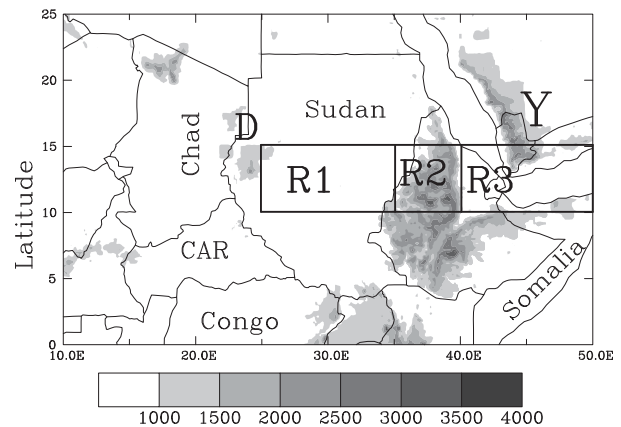

FIG. 1. Central and East Africa (elevation ≥ 1000 m are shaded). Boxes R1 (10°–15°N, 25°–35°E), R2 (10°–15°N, 35°–40°E; Ethiopian highlands), and R3 (10°–15°N, 40°–50°E) denote the study areas where transition in weather states appear to occur (MR11; see text for details). The major highlands in the region are the Darfur Mountains (denoted by D; just northwest of R1), the Ethiopian highlands (R2), and the Yemen highlands (denoted by Y; north of R3).

of the highlands. MR11 speculated that the transition from less organized to well-organized convective type facilitates the main AEW initiation pathway, summarized as WS3 → WS1 → AEW: in this case the enhanced heating by WS1 serves as the diabatic heating studied by Thorncroft et al. (2008). There is also a potential for an alternate pathway: WS3 → AEW → WS1. That is, wave disturbances may evolve from a WS3 type of convective activity and then, the AEWs create a favorable environment for WS1 development. MR11 did not investigate this pathway. We investigate the WS3 → AEW → WS1 pathway and its association with a low- to midlevel shear environment.

Westerlies in the lower troposphere and easterlies in the mid- and upper troposphere dominate the July–August–September (JAS) flow pattern over East Africa, suggesting a role of vertical zonal wind shear. Observational and numerical model studies suggest that vertical wind shear enhances deep convective organization (e.g., Laing et al. 2008; Moncrieff 1981; Grabowski and Moncrieff 2004; Anber et al. 2014). The high terrain in East Africa is a source of elevated heating, which tends to increase vertical shear and horizontal vorticity (e.g., Grabowski and Moncrieff 2004). Therefore, WS3 activity might increase in association with increased vertical wind shear and vorticity development and these may initiate wave perturbations first. Then, wave development and further clustering of WS3 aided by elevated heating might result in the growth of larger and well-organized convection, WS1. This study investigates the two different pathways using 25 years of data.

Recently Janiga and Thorncroft (2016) presented a comprehensive analysis of AEW phases and different properties of convection using reanalysis and precipitation from the Tropical Rainfall Measuring Mission. However, they did not investigate the interaction between different types of deep moist convection and AEWs.

The diurnal cycle of deep convection and its interaction with AEWs over tropical Africa was investigated by Laing et al. (2008). They performed their analysis using cold-cloud brightness temperature T_B and used 233 K as a threshold for precipitation, assuming that cloud $T_B < 233$ K is more likely to be precipitating. Several others (e.g., Duvel 1989) have also used such T_B thresholds to analyze deep convection over Africa. However, the nature of different types of deep convection cannot be understood using T_B as it is not capable of distinguishing different types of deep convection. Moreover, T_B mixes different weather states (MR11). The easternmost domain used by Laing et al. (2008) is 40°E and convective processes farther east were not explored. The deep convective propagation from the Yemen highlands and adjoining Arabian Sea has an important impact on the summer moist convection and rainfall over the Ethiopian highlands (Fig. 1; Segele and Lamb 2005; Viste and Sorteberg 2013). We expand the work by Laing et al. (2008) by applying the ISCCP WS data and expanding the domain to include the region east of the Ethiopian highlands to understand the role of diurnal variations in the initiation of AEWs.

Understanding the transition process requires detailed study of the atmospheric states over East Africa. The large-scale mechanisms that determine AEW initiation over East Africa, including the vertical wind shear (e.g., Laing et al. 2008, 2011), require investigation. Additionally, East Africa is characterized by complicated topography (Fig. 1), which may have an important role in wave disturbances and convection. East African mountains exhibit a significant diurnal variability, explaining an important portion (~30%) of the total convective variance during JAS (e.g., Mekonnen et al. 2006; Yang and Slingo 2001). The role of the diurnal cycle on WS transition was not explored in the past studies cited here.

Past work suggested that MCSs are generated in association with topography (e.g., Laing and Fritsch 1993), while another study suggested that MCSs and squall lines over West Africa are strongly impacted by AEWs (e.g., Fink and Reiner 2003). However, the role of large-scale deep convection on AEWs is still not well understood. A suite of multiple satellite and reanalysis datasets will be used to investigate the association between different types of deep convection and AEWs

including the role of large-scale dynamics. Results from this study are summarized based on three regions in East Africa identified in Fig. 1 as R1 (10°–15°N, 25°–35°E), R2 (10°–15°N, 35°–40°E), and R3 (10°–15°N, 40°–50°E). R1 is located in central and eastern Sudan and is the region where WS1 is shown to peak in MR11. Also, a significant 3–4-day periodic oscillation in T_B was shown in this region previously (e.g., Mekonnen and Thorncroft 2016; Mekonnen et al. 2006). R2 denotes the Ethiopian highlands. R3 represents the region east of Ethiopian mountains including the southern Red Sea and parts of Yemen where the WS3 anomaly is shown to peak (MR11; cf. Fig. 3 below).

2. Data and analysis methods

a. Data sources

1) ISCCP WEATHER STATE (WS) AND INFRARED WS (IR-WS) DATASETS

ISCCP provides a number of different satellite-based cloud products. The 3-hourly, global gridded (2.5° equivalent equal area) product reports cloud, atmosphere, and surface properties, including a joint histogram describing the distribution of cloud-top pressure (CTP) and optical thickness τ in each grid cell (Rossow and Schiffer 1991). The D-version of this product (ISCCP D1; Rossow and Schiffer 1999) is available for the period July 1983–December 2009. Pattern analyses of these histograms (Jakob and Tselioudis 2003; Rossow et al. 2005) identified six different characteristic WSs in the tropics (15°S–15°N), three of which represent convectively active situations and three of which represent inactive (suppressed) situations. Subsequent studies used an extended tropics (35°S–35°N) version that includes two more suppressed WSs to examine the relationship of AEW initiation and deep convection (e.g., MR11). An extended tropics dataset together with southern (65°–35°S) and northern (35°–65°N) midlatitude sets were used to study cloud effects on the radiation budget (Oreopoulos and Rossow 2011). Past studies show a switching behavior between different types of convective WSs (Jakob and Tselioudis 2003; Jakob et al. 2005; Tromeur and Rossow 2010, MR11). The precipitation rate associated with different types of WSs is also different (Lee et al. 2013; Rossow et al. 2013). Tselioudis et al. (2013) found a characteristic association between cloud vertical structure and large-scale vertical motions with each WS.

Figure 2 shows the joint CTP–τ histograms that define the extended tropical WS. The fractional areal coverage of each mesoscale domain by each pair of CTP–τ values
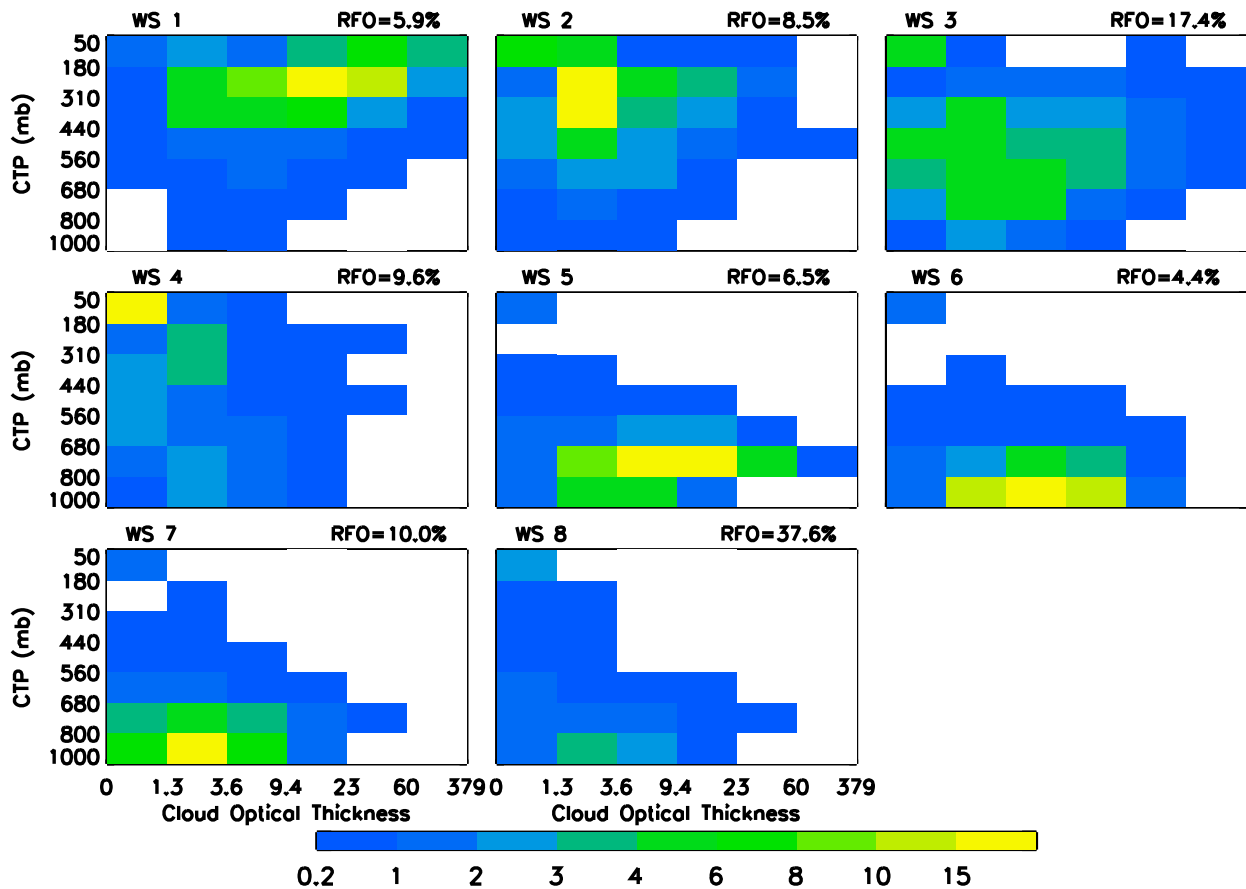
FIG. 2. Mean CTP–τ patterns of eight weather states (WSs) from 3-hourly ISCCP D1 data (colors in legend indicate fractional coverage of the 2.5° map grid cell). The histogram is the 1983–2004 average for latitudes 35°S–35°N. The WS, numbered 1–8, describe from (top) most convectively active to (middle),(bottom) least convectively active states. The WS relative frequencies of occurrence (RFO; in %) are shown on the top-right corner of each plot (see text for details; from MR11).

is indicated by the colors. The thicker ($\tau > 23$) and higher-topped (CTP < 440 hPa) clouds are associated with deep convection, and the moderately thick and higher-topped clouds are related to mesoscale anvil clouds. Higher-topped but optically thin clouds on the top-left side of the histograms denote cirrus clouds. The relative frequencies of occurrence (RFO) for each WS over the 35°S–35°N domain are shown at the top-right corner of each plot (averaged over the whole data record). Although less frequent (RFO = 5.9%) in the tropics, WS1 has the largest area covered by deep convective clouds (as indicated by the color scale) and is identified as mesoscale cloud systems (MCS). WS2 (RFO = 9%) has fewer deep convective clouds and more anvil clouds but these two WS generally occur together (cf. Jakob and Tselioudis 2003; Rossow et al. 2005; Tromeur and Rossow 2010), indicating that they are different parts of cloud systems that are larger in size than the 2.5° domain. WS3 (RFO = 17.4%) contains a smaller fraction of deep convective clouds mixed with

cirrus and other lower-level clouds, but they are still associated with significant precipitation compared to the suppressed WS and are identified as smaller-scale ordinary cumulonimbus. Thin cirrus and scattered cumulus dominate WS4 (RFO = 9.6%) and shallow boundary layer clouds dominate WS5–WS8, indicating convectively suppressed conditions.

This study focuses on the diurnal variations of convection, using another WS dataset, the infrared WS (IR-WS), based solely on infrared (IR) measurements. The WS described above are defined only in the daytime when τ retrievals are available. The ISCCP D1 data also provide CTP histograms for each grid cell at all times of day, where the retrievals use only infrared information and assume all clouds are blackbodies. By compositing these CTP histograms for each daytime WS defined by CTP–τ, Tan et al. (2013) produced IR-WS (a.k.a. cloud regimes). They found three distinct convectively active and four convectively suppressed states. Their convectively active states (called CD, CC, and IM)

IR−WS1/all (1983−2009)

IR−WS2/all (1983−2009 JAS)

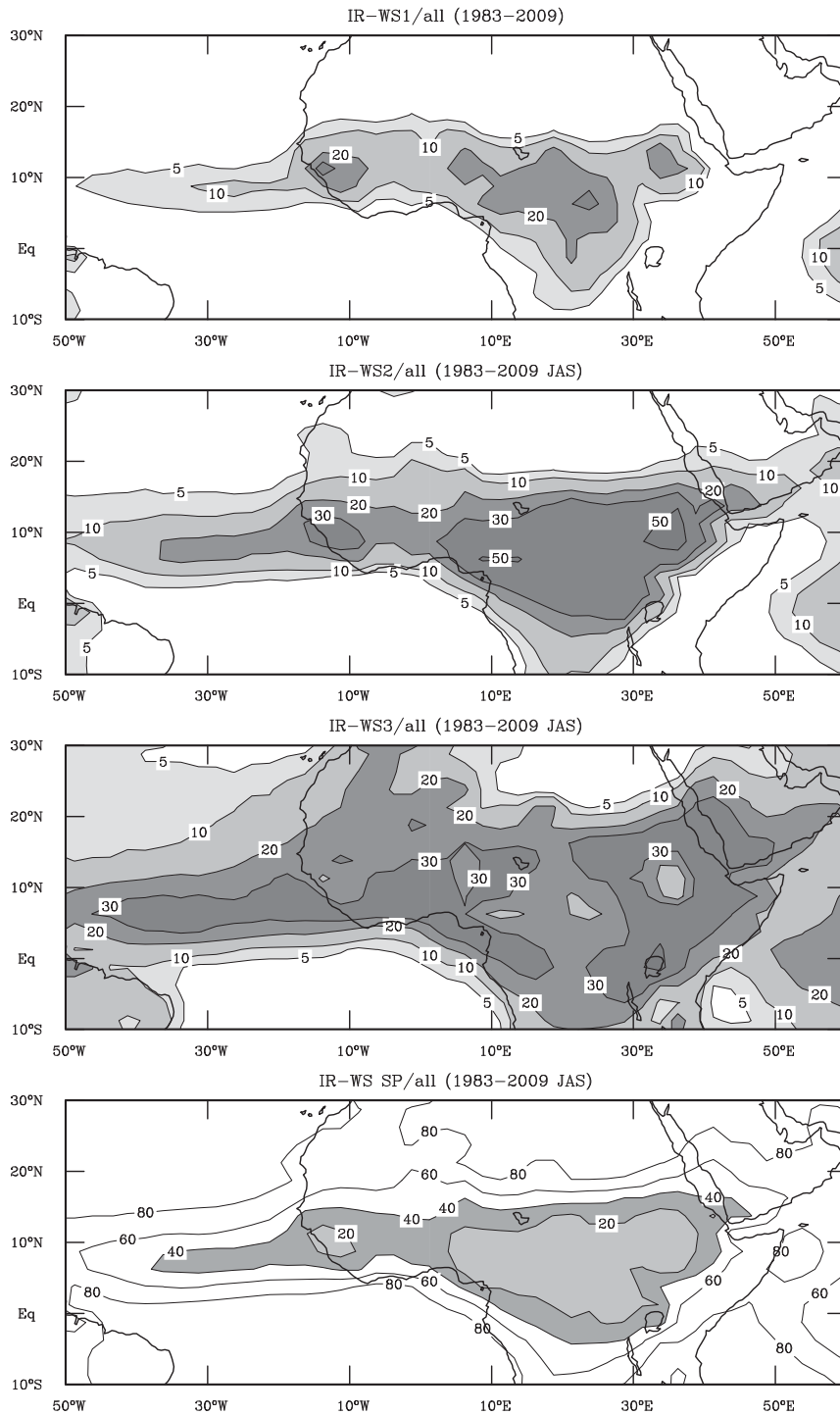IR−WS3/all (1983−2009 JAS)

IR−WS SP/all (1983−2009 JAS)

FIG. 3. The geographic distribution of IR-WS averaged for July–September 1983–2009. Percentages are with respect to the total frequency of all cloud occurrences. The first three panels present different types of convectively active regimes, while the bottom panel presents suppressed regimes (see text for details).

correspond to the three daytime WS (WS1, WS2, and WS3), described above, and exhibit similar RFO values. Tan et al.'s classification also includes thin cirrus (IC), equivalent to WS4, and three low-level cloud types indicating suppressed conditions (they have fewer suppressed cases because IR retrievals for low-level clouds cannot discriminate different optical thicknesses very well). Therefore, the IR-WS states are WSs extended for nighttime. For consistency, we use the following terminology: IR-WS1 = CD, IR-WS2 = CC, IR-WS3 = IM, IR-WS4 = IC, and suppressed convective regimes, IR-WS SP = (SP5 + SP6 + SP7 + SP8). The IR-WS dataset is available at 2.5°, 3-hourly from 1983 to 2009 for the extended tropics (35°S–35°N).

Figure 3 shows the JAS geographic distribution of the IR-WS. The higher frequencies of the convectively active cloud systems (IR-WS1, -2, and -3) coincide with seasonal location of the deep convective zone. Higher frequencies of the suppressed cloud systems are concentrated outside of the deep convective zone. IR-WS1 and IR-WS2 are much less frequent than IR-WS3, but most of the rainfall is associated with them (cf. Lee et al. 2013; Rossow et al. 2013). The peak IR-WS3 frequency is located just to the east of the peak IR-WS1 and IR-WS2 in East Africa in agreement with Semunegus et al. (2017, see their Fig. 1). We will show below that this is the key aspect of "transitioning" between different types of deep convection that have been given little attention in the past.

There is a close association between WS1 and WS2 (or IR-WS1 and IR-WS2), where the former is the core and the latter is the mesoscale anvils of large mesoscale systems. Thus, we apply the combined occurrences, IR-WS1 + 2, to match the rainfall datasets below.

2) TRMM TMPA 3B42, VERSION 6, DATASET

The Tropical Rainfall Measuring Mission (TRMM) Multisatellite Precipitation Analysis (TMPA) is a product of various satellite observations and precipitation gauge measurements over land. It is available at 0.25° covering 50°S–50°N, and at 3-hourly time intervals. We use the period 1998–2008. Our study includes IR-WS matched rainfall analysis. Since IR-WS and TMPA are at different horizontal grid resolutions, we regrid TMPA into 2.5° × 2.5° (Rossow et al. 2013). More details about TMPA can be found in Kummerow et al. (2000) and Huffman et al. (2007) and others.

Here, IR-WS matched rainfall is prepared to examine the contribution of different IR-WSs to the JAS rainfall. For each grid point and each time step only one type of IR-WS is present. That means if one of the IR-WS is present (identified by a number >0), the rest are absent (assigned 0) unless that particular grid point and time

step is characterized by a missing data or clear-sky condition. Assignment of IR-WS for each grid point and each time is unique and there is no double counting or duplication. Therefore, for each grid point and each of the 3-hourly time steps, if a particular IR-WS is present, we assume that the corresponding rainfall is due to that particular IR-WS. Since the assignments are unique, the contribution of other weather states to the rainfall is zero. If the TMPA rainfall is missing, then the corresponding IR-WS matched rainfall is also neglected. Rossow et al. (2013) describe further details of composite techniques using occurrences in WS.

Rossow et al. (2013) matched different WSs in the global tropics to the total observed TMPA data and discussed the relative contribution of each WS to the observed rainfall. They showed that most of the tropical precipitation is explained by WS1 and WS2. Similarly, Jakob and Schumacher (2008) showed that the largest contribution to the rainfall over the tropical western Pacific region comes from WS1-type convection. Figure 4 presents the geographic distribution of JAS (1998–2008) TMPA rainfall that is matched by IR-WS1 + 2, IR-WS3, and IR-WS SP. Most of the season's rainfall is associated with IR-WS1 + 2, consistent with the findings in Rossow et al. (2013). The IR-WS3 matched TMPA rainfall also contributes to the seasonal total, although by a small amount. Peak rainfall pockets are observed in the vicinity of eastern and western highlands. Rainfall associated with the suppressed cloud regimes (IR-WS SP) is small (third panel). IR-WS1 + 2 and IR-WS3 matched rainfall together explain the seasonal mean rainfall of the region. As in Fig. 3, the IR-WS3 matched rainfall peak over East Africa is slightly to the east of the IR-WS1 + 2 matched rainfall.

3) INFRARED COLD CLOUD BRIGHTNESS TEMPERATURE (T_B)

The IR-WS data are presented in discrete formats and a direct application of filtering techniques to separate convective variability in various ranges will not be suitable. Instead, we use T_B to study the role of diurnal cycle on AEW initiation. The T_B is compiled based on ISCCP B3 products in 10–12-μm infrared windows (Hodges et al. 2000), which originally has a spatial sampling of 25–30 km. The T_B is obtained from the Cloud Archive User Service project of the European Union via the U.K. Centre for Environmental Data analysis (http://data.ceda.ac.uk/badc/claus/data/channel_2/lo_res/). The T_B is available at 0.5° global horizontal grid, at 3-h intervals, and for the period 1984–2008. More details of T_B data can be found in Hodges et al. (2000).
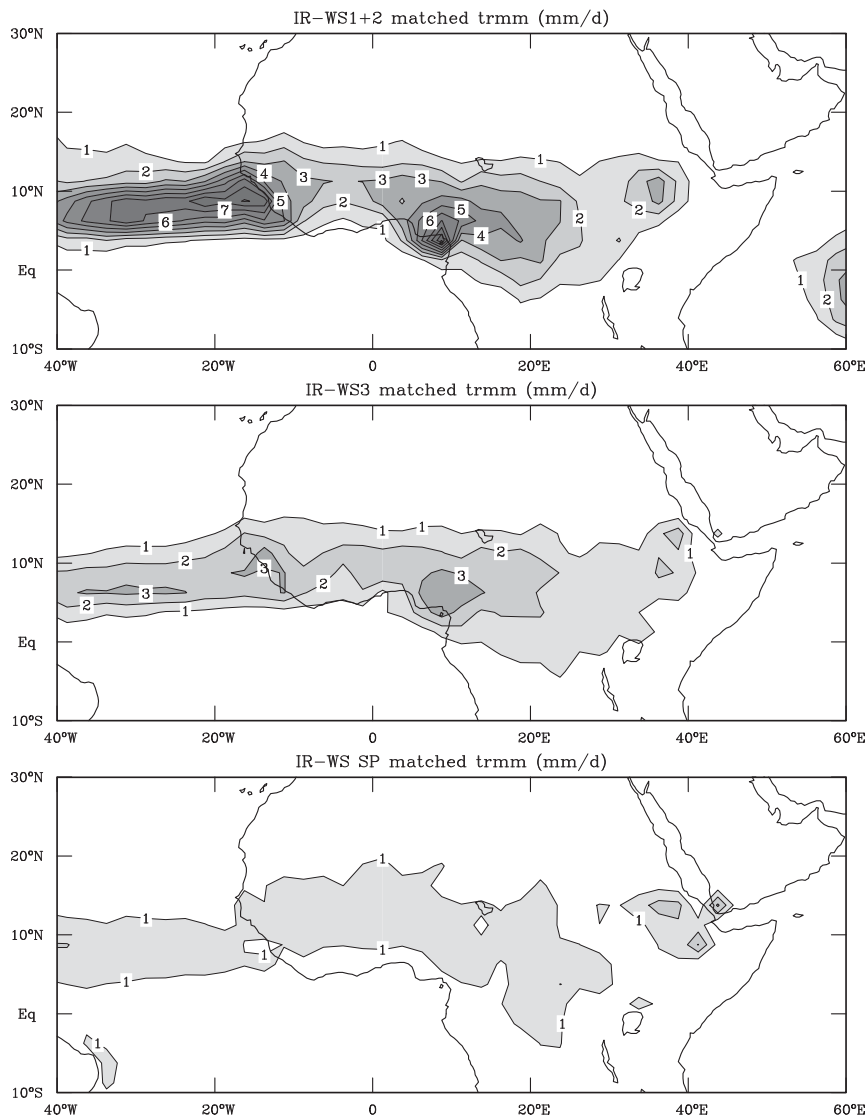
FIG. 4. IR-WS matched TRMM rainfall for JAS 1998–2008: (top) matched with IR-WS1 + 2, (middle) matched with IR-WS3, and (bottom) matched with IR-SP (suppressed regimes).

4) ERA-I DATA

Atmospheric variables such as wind, equivalent potential temperature θ_E, relative vorticity, and specific humidity are obtained or computed from ECMWF interim reanalysis (ERA-I) products. Observational data over East and central Africa is sparse. In addition, it is known that the model physics underlying the reanalysis lacks a representation of MCS (e.g., Tompkins et al. 2005) and hence, anomalies of variables such as vertical velocity should be interpreted with caution. Despite sparse data and the inadequacy of representing meso-scale convection, past work (e.g., Tompkins et al. 2005) suggests that the reanalysis products still offer a good

estimation of synoptic-scale environments. We use ERA-I at 1.5° global horizontal grid, 6-h intervals, and for the period 1984–2008. The ERA-I products are available at 37 pressure levels and for various grid intervals starting from 1979 to the present. More details of ERA-I can be found in Simmons et al. (2007) and Dee et al. (2011). ERA-I is obtained from the ECMWF (http://www.ecmwf.int/).

b. Analysis methods

Lanczos filtering (Duchon 1979) is used to separate different ranges of variability. The role of diurnal variance is studied using high-pass filtering with a 1.125-day cutoff on 3-h T_B data. Synoptic-scale variability is
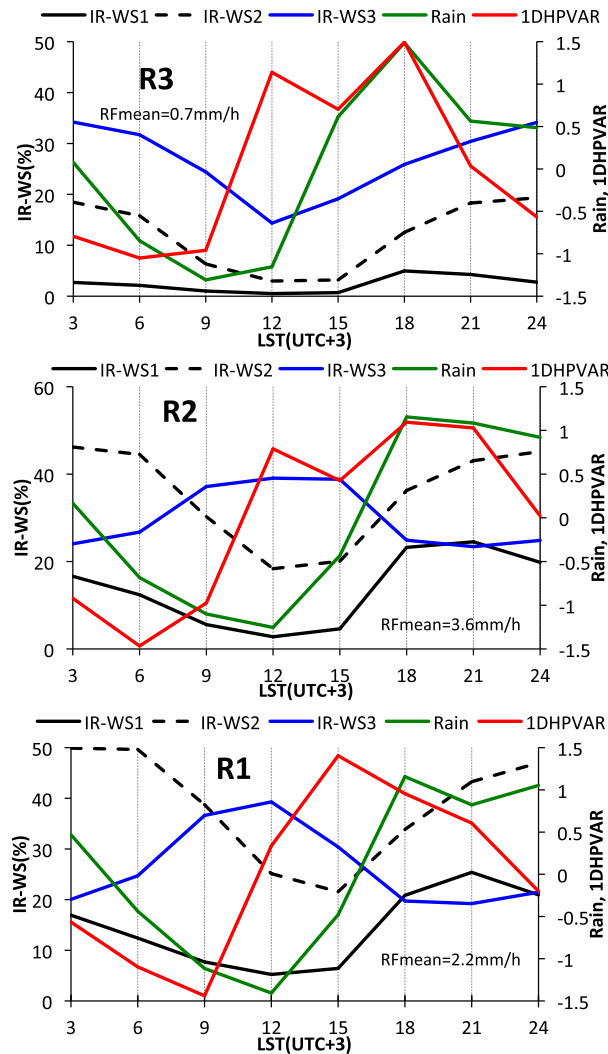
FIG. 5. The mean diurnal evolution of different convective cloud regimes (IR-WS 1–3), total rainfall, and intradiurnal variance anomalies (1DHPVAR; K^2) during JAS over R1, R2, and R3. The vertical axis on the left shows the percentage frequency of the total cloudiness. The vertical axis on the right shows rainfall and intradiurnal variance anomalies standardized with their respective standard deviations. The rainfall totals are based on $1° \times 1°$ horizontal grid. The abscissa is in local standard time (UTC + 3 h). Mean daily rainfall and mean diurnal variances are subtracted from each to form anomalies. Daily rainfall averages are indicated for each region.

examined using bandpass filtering in the 2–10-day interval. To sharpen the response of the filter, 30-day data points are used before and after the time series to be filtered. Composite analyses are performed using a linear regression method as in Wheeler et al. (2000).

Regression composites are prepared for total fields (e.g., wind, IR-WS, and vorticity) correlated and regressed against the filtered time series at a chosen base point and results are presented in the form of anomalies scaled by one standard deviation of the base point time series. Details on the method of regression compositing can be found in past papers (e.g., Kiladis et al. 2006; Wheeler et al. 2000).

As described in section 2a(3), the IR-WSs are presented in discrete formats. Therefore, for regression composites, we converted the discrete numbers into frequency of percent during a day. If a particular IR-WS is present at a given time and space, its assigned value is 12.5% ($=1/8 \times 100$), while all other IR-WS types are assigned 0%.

3. The climatology of diurnal cycle and low-level wind shear over East Africa

AEW initiation over East Africa is related to organized mesoscale convection. Major mechanisms and circulation features that impact deep convection over East Africa include moist low-level westerlies and southerlies originating from the southern Atlantic and southern Indian Oceans and mid- and upper-tropospheric easterlies. The monsoon trough, where low-level northerlies and southerlies converge, is located north of the study area near 20°N, while the deep convective zone is situated south of the monsoon trough (e.g., Mekonnen and Thorncroft 2016, see their Fig. 2; Nicholson 2018).

Most of the convective activity over the region exhibits intradiurnal (≤ 1 day) variance (e.g., Mekonnen et al. 2006; Yang and Slingo 2001). Deep convective development and growth is influenced by several factors. Past studies have shown that the diurnal cycle and vertical wind shear significantly influences convective development. To provide context, we briefly discuss the climatology of the diurnal cycle and the 600–850-hPa (low level) wind shear over the study area.

a. The diurnal cycle

The climatology of the diurnal cycle is illustrated using three different types of deep convection (IR-WS1, IR-WS2, and IR-WS3) and TMPA rainfall. The diurnal cycle of convection is represented using high-pass-filtered T_B at 1.125 day and the intradiurnal variance (a.k.a. the intradiurnal activity) is computed based on this filtered data (Yang and Slingo 2001). Figure 5 presents the mean diurnal cycle of IR-WS1, IR-WS2, IR-WS3, the intradiurnal variance, and rainfall over three regions R1, R2, and R3 (Fig. 1) in local standard time (LST). The original $0.25° \times 0.25°$ TMPA rainfall is regridded to $1° \times 1°$ grid total areal rainfall for this figure (Rossow et al. 2013).

1) DIURNAL VARIANCE IN R3

IR-WS1-type clouds are infrequent (<5% of total cloudiness) over this region (cf. Fig. 3; Semunegus et al. 2017). Evolution of IR-WS1 shows a slight increase later in the afternoon. IR-WS2 increases between 1500 LST and late night, peaking 3 h after IR-WS1. IR-WS3 appears to increase starting at midday and peaks late in the night. The intradiurnal activity (denoted by 1DHPVAR; Fig. 5) peaks between local noon and 1800 LST, but sharply declines after 1800 LST. The intradiurnal activity peaks ahead of the convective clouds (IR-WSs). Region R3 is a low-rainfall zone (mean = 0.7 mm h^{-1}) and is located on the eastern side of the Ethiopian mountains (cf. Fig. 4). Even though small, the positive anomaly of rainfall increases between 1500 and 1800 LST and decreases after that.

2) DIURNAL VARIANCE IN R2

IR-WS1 clouds are at a minimum until 1500 LST, but increase sharply between 1500 and 2100 LST (~25% of total cloudiness at peak time). IR-WS2 appears to follow the IR-WS1 and peaks 3 h after the IR-WS1. IR-WS3 increases between 0900 and 1500 LST, but sharply decreases after that. IR-WS3 fluctuates opposite to IR-WS1. A sharp decrease of IR-WS3 in the afternoon may be explained by the process of merging of scattered convective clouds to form larger and well-organized clouds during the course of the day. Deep large-scale convection peaks in the afternoon in response to the daytime heating (cf. Parker et al. 2005). The intradiurnal variance peaks between 1200 and 2100 LST. Maximum intradiurnal activity precedes maximum IR-WS1, suggesting a role of intradiurnal variance in increasing deep and larger-scale convection. Generally, the intradiurnal variance fluctuates in phase with IR-WS1 and IR-WS2. Also, the rainfall increases in phase with IR-WS1 and peaks during the maximum IR-WS1 and IR-WS2 period.

3) DIURNAL VARIANCE IN R1

IR-WS1 increases between 1500 and 2100 LST. IR-WS2 increases from midday to late night, following IR-WS1. IR-WS3 increases before noon but sharply falls after that. Maximum intradiurnal activity occurs at 1500 LST, about 3 h before maximum IR-WS1. Rainfall increases in the afternoon and peaks around 1800 LST, gradually decreasing after that and becoming closer to zero around midday. Both IR-WS1 and rainfall peak between 1800 and 2100 LST. It is seen that the rainfall fluctuates in phase with IR-WS1.

The above observations are consistent with past work that show increased deep moist convection occurring later in the day and into the evening hours (e.g., Parker et al. 2005). However, discriminating between the different types of convection shows that the increase in deep convection appears as a transition of IR-WS3 earlier in the day to IR-WS1 and IR-WS2 later in the day and that this transition is associated with a significant increase in rainfall. Peak intradiurnal variance precedes well-organized convection, suggesting an important influence on development of the deep convection. The different diurnal phases seen above may be the key to understanding the role of different types of deep convection.

b. *The 600–850-hPa (low level) vertical wind shear*

The African easterly jet (AEJ) is a major feature of the North African summer monsoon. AEJ owes its existence to the lower-level north–south meridional temperature gradient between cooler equatorial Atlantic in the south and the hot Sahara in the north, which is proportional to the vertical easterly wind shear. Past work (e.g., Laing et al. 2008) suggested that organized convection over the tropical North Africa is associated with the AEJ environment and with the wind shear between 600 and 925 hPa. East Africa is mainly dominated by high terrain more than 1000 m (Fig. 1) and the 925-hPa level is at or below the ground. We use the 850-hPa level instead (Fig. 6). The 600-hPa mean zonal wind axis (i.e., AEJ) is also superimposed for comparison. The shear structure follows the AEJ, while the wind shear axis lies slightly to the north of the AEJ axis. The moderately strong wind shear values (10–14 m s^{-1}) are located in East and West Africa, while relatively low shear (<10 m s^{-1}) occurs in central Africa between 15° and 20°E. The strongest shear magnitudes (>20 m s^{-1}) are located east of the Ethiopian highlands, over the southern Red Sea, and western Indian Ocean. The shear vector direction is generally northeasterly over East Africa and easterly over West Africa, similar to the results in Laing et al. (2008). The moderate magnitude and general direction of wind shear in West and East Africa suggests the presence of a favorable environment for mesoscale convection (cf. Laing et al. 2008). In contrast, the strong and north-northeasterly wind shear east of the Ethiopian highlands can initially favor isolated and less well-organized convection (scattered thunderstorm) development, but may not support a sustained growth of well-organized mesoscale convection as the region is on the leeward side of the low-level flow (Mekonnen and Thorncroft 2016). Also moderate shear and the presence of large convective available potential energy (CAPE) is a favorable environment for intense convection (e.g., Mohr and Thorncroft 2006). The climatology of CAPE (not shown) indicates that large CAPE is confined
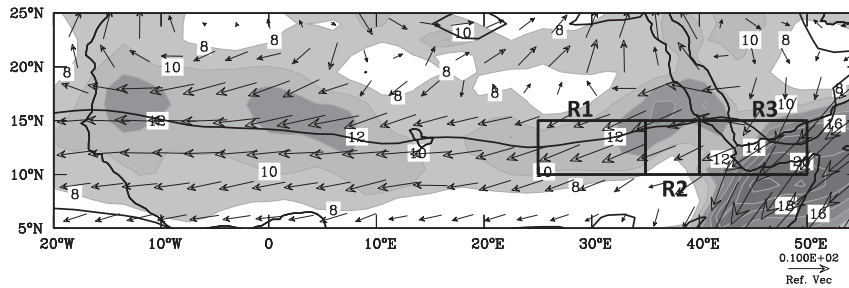
FIG. 6. The mean wind shear between 600 and 850 hPa (magnitude shaded every $2 \, \mathrm{m \, s^{-1}}$ starting from $8 \, \mathrm{m \, s^{-1}}$) for JAS 1984–2008. The 600-hPa mean zonal wind axis ($\overline{U}_{600\mathrm{MAX}}$; AEJ) is also shown for reference (denoted by west–east heavy solid line). The 600–850-hPa shear magnitude is calculated as $|\mathbf{V}| = [(U_{600} - U_{850})^2 + (V_{600} - V_{850})^2]^{1/2}$, without dividing the result by depth between the two levels. Boxes in East Africa denote regions (from left to right) R1, R2, and R3 as in Fig. 1.

around the Ethiopian mountains, while the region to the east is characterized by low CAPE, suggesting that the region east of the Ethiopian highlands is not favorable for MCS activity.

4. Results and discussion

Next, we investigate AEW initiation pathways and weather state transitions. Of particular interest are the following mechanisms: the dynamic and thermodynamic processes including the diurnal cycle that potentially determine the transition. The results are presented on 6-h time steps, when reanalysis is involved and on 3-h intervals when using results other than reanalysis. Unless indicated otherwise, our analysis is based on composites using 2–10-day-filtered 700-hPa meridional wind time series at base point 12.5°N, 32.5°E in East Africa. The reason for choosing this location is because the WS transitions discussed above occur in the region. The bandpass-filtered 700-hPa meridional wind is used as a key indicator of AEWs (e.g., Albignat and Reed 1980; Thorncroft and Hodges 2001). Regression composite anomalies in this section are departures with reference to the long-term mean. Results summarized in Figs. 7–10 (see below) present weather state transitions, diurnal cycle activity, and thermodynamic and dynamic processes that may explain the WS transitions. Results are presented based on the three regions in East Africa indicated in Fig. 1.

a. The role of diurnal cycle

The role of diurnal cycle is examined by projecting the intradiurnal variance onto the 2–10-day-filtered 700-hPa meridional wind time series. Figure 7 presents the regression composite anomalies of IR-WSs and intradiurnal activity for the three East African regions, every 6 h, from day −4 to day +4.

1) REGION R3

The IR-WS1 types are infrequent and the anomalies are nearly zero, consistent with earlier findings (Figs. 3, 5). Intradiurnal activity peaks between day −1 and day −0.5. IR-WS2 and IR-WS3 peak at day −0.5, shortly after the peak diurnal activity. The intradiurnal activity fluctuates in phase with IR-WS3. The peak intradiurnal activity preceding IR-WS3 suggests that the diurnal cycle influences IR-WS3 more than IR-WS1 in this region. As shown in Fig. 4, IR-WS3-related rainfall peaks in R3, but is smaller over R2.

2) REGION R2

Intradiurnal activity peaks around day −0.75. IR-WS1 peaks at day 0. IR-WS2 peaks around day +1.5, following IR-WS1. IR-WS3 peaks at day −1.5, but sharply falls to a minimum at day +0.5. IR-WS3 peaking before IR-WS1 and weakening during the increasing period of IR-WS1 suggests merging and organization of smaller-scale convection into larger-scale deep convection. The peak intradiurnal activity leading IR-WS1 suggests an important influence of diurnal activity in enhancing large-scale convection.

3) REGION R1

The amplitudes of variables in this region are larger than those in R2. Intradiurnal activity over R1 peaks around day −0.5. IR-WS1 peaks at day 0 and IR-WS2 peaks later following IR-WS1. IR-WS3 peaks at day −2.25 and falls to a minimum at day −0.25, almost out of phase with the fluctuation of IR-WS1. Maximum intradiurnal activity before maximum IR-WS1 indicates that the intradiurnal activity influences deep convection. The intradiurnal activity over R1 peaks before the maximum intradiurnal activity over R2, suggesting that the activity starts over the Ethiopian highlands and propagates westward.
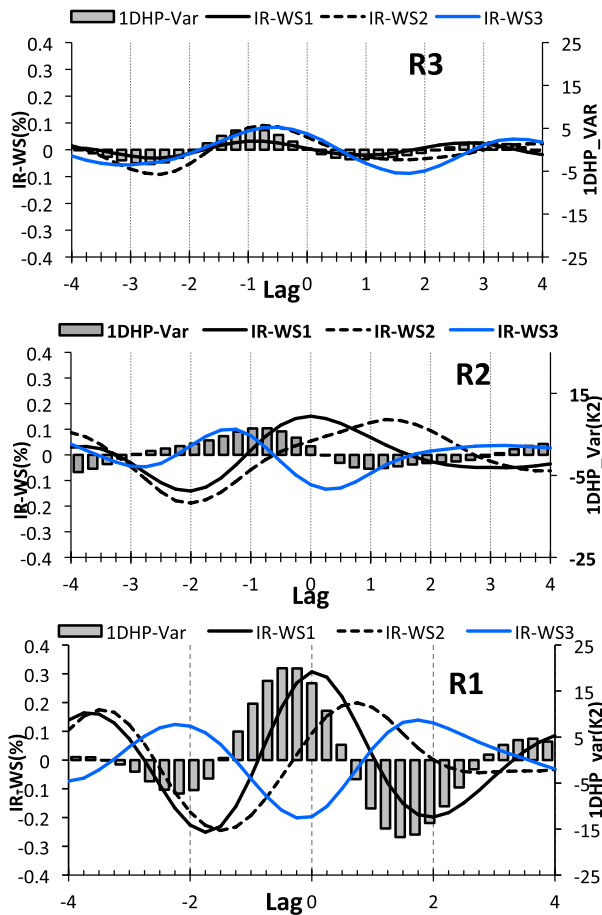
FIG. 7. The regression composite anomalies of intradiurnal variance (1DHP-Var; shaded bar graphs; K^2), IR-WS1 (solid black lines), IR-WS2 (dashed black lines), and IR-WS3 (blue lines) for the three regions, R3, R2, and R1 in East Africa. IR-WSs (left y axis) are expressed in percent. Anomalies of intradiurnal activity are indicated on the right y axis. Lags are every 0.25 days (6 hourly). Regressions are based on 2–10-day 700-hPa meridional wind at 12.5°N, 32.5°E.

Comparison of the evolution and timing of the peak frequency of IR-WS1 over R1 and R2 shows that well-organized convection starts over the Ethiopian highlands where intradiurnal activity appears to play an important role and increases westward and maximizes over R1. This is consistent with observations of past work that attribute AEW initiation to large-scale deep convection over the region between the Darfur Mountains and the Ethiopian highlands (e.g., MR11; Kiladis et al. 2006; Lin et al. 2005).

b. Thermodynamic processes: Atmospheric instability and moisture

We use the 850-hPa equivalent potential temperature θ_E to describe atmospheric instability. We also use the

850-hPa specific humidity q to evaluate the potential for deep convection in association with increasing atmospheric instability. Composite anomalies are formed by projecting the 6-hourly θ_E and q onto the basepoint time series described above. Figure 8 shows the evolution of θ_E and q at 850 hPa for lag days −4 to +4 for the three regions in East Africa. IR-WS1, IR-WS2, and IR-WS3 composite anomalies are also reproduced for comparison.

1) REGION R3

The θ_E anomaly increases (implying a more unstable atmosphere) between day −2.5 and day −1 and its peak amplitude precedes the peak IR-WS3. The amplitude of the q anomaly is small, fluctuating around zero. Although θ_E indicates a relatively unstable atmosphere, lack of moisture appears to limit deep convective development over R3 and may explain the infrequent development of the IR-WS1 type of deep convection (cf. Fig. 3).

2) REGION R2

The θ_E anomaly increases starting at day −2.5 and peaks at day −0.75. Peak positive θ_E precedes maximum IR-WS1 by about 18 h and maximum IR-WS2 by about 2 days. However, maximum θ_E lags IR-WS3 by about half day. Similarly, q anomalies increase between day −2 and −0.75, preceding the maximum IR-WS1 but following the increase of IR-WS3. Increasing convective instability (positive θ_E) and humidity in the lower level of the troposphere ahead of large MCS convection are consistent with earlier observations for West Africa (e.g., Kiladis et al. 2006). The sequence of events over R2 indicates IR-WS3 → θ_E, q → IR-WS1 → IR-WS2.

3) REGION R1

The fluctuation of θ_E over R1 is opposite to that over R2. It decreases between day −2 and day −0.5, while IR-WS1 increases and peaks at day 0. The term θ_E increases again after maximum IR-WS1 and peaks at day +1.5. The fluctuations of IR-WS1 and θ_E are out of phase over this region. The amplitude of IR-WS1 over R1 is greater than over R2. A Hovmöller analysis (not shown) of IR-WS1 suggests that the large-scale convection that starts over the Ethiopian mountains moves westward toward R1 and grows deeper and covers a larger area. Although decreasing θ_E over R1 before maximum IR-WS1 implies a decreasing instability situation in the lower troposphere, the frequency of IR-WS1 increases. Decreasing θ_E before day 0 in this region may be offset by increased elevated heating by IR-WS1 over the Ethiopian mountains so that the atmosphere remains unstable. On the other hand, the figure
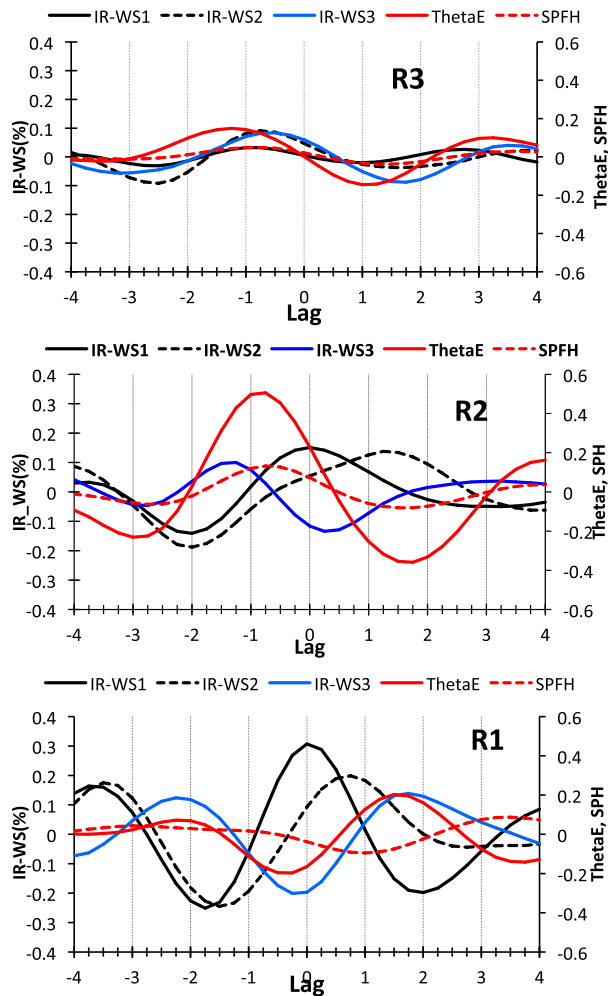
FIG. 8. The regression composite anomalies of equivalent potential temperature (θ_E; K; red line), specific humidity (q; g kg^{-1}; red dashed line), and IR-WSs (%) over East African regions. The ordinate on the right is for IR-WS and the one on the left is for θ_E and q. Regression composites are as in Fig. 7.

shows θ_E peaking over R1 at day +1.5 following maximum IR-WS1. This might suggest that the role of strong environmental heating through deep convection tends to perturb the atmosphere downstream of the highlands, which may lead to AEW initiation. IR-WS3 drops to a minimum around day 0 and peaks at day +1.5. This implies the organization of IR-WS3 into IR-WS1 at or before day 0 and, when well-organized convection starts weakening, the frequency of isolated less well-organized convection increases again.

As shown in Fig. 8, increasing θ_E precedes the increasing frequency in IR-WS1 (MCS activity) over the Ethiopian highlands (R2), suggesting an important role of increasing atmospheric instability in the lower troposphere, an important condition for convective

development and growth. Additionally, increasing q anomaly indicates the increasing low-level moisture availability. IR-WS3 peaks before maximum IR-WS1 over R2. Increasing IR-WS3 before IR-WS1 might contribute, in part, to the moistening of the middle atmosphere (IR-WS3 is a combination of midlevel and vertically growing deep clouds including scattered cumulonimbus; Fig. 2; e.g., Tromeur and Rossow 2010). However, the details of the moistening process are beyond the scope this study. Increasingly unstable atmosphere together with increasing moisture in the midlevels of the troposphere are favorable conditions for deep convection growth. IR-WS1 decreases after day 0 over R2, and atmospheric instability decreases (decreasing θ_E). The decrease in θ_E after peak convection is, perhaps, due to convective downdrafts, that tend to stabilize the local atmosphere. IR-WS3 increases between lag day −2.5 and lag day −1.5, but sharply decreases after that over the highlands. The evolution of θ_E and IR-WS3 appears to be similar until day −1.5 but switches out of phase after day −1.5. This suggests that the increasing instability environment continues to favor larger-scale and well-organized convection as opposed to scattered and small-scale convection over the Ethiopian highlands. IR-WS3 clouds peak some 2.5 days before maximum IR-WS1 and the transition from IR-WS3 to IR-WS1 appears to start about 30 h before the maximum large-scale convection. Thus, the thermodynamic processes over R1 and R2 indicate a transition of IR-WS3 to IR-WS1 that occurs primarily over the Ethiopian highlands.

c. Dynamical mechanisms

1) THE ROLE OF LOW- TO MIDTROPOSHERIC WIND FLOW AND RELATIVE VORTICITY

The JAS circulation over tropical North Africa features westerlies and southwesterlies in the lower troposphere, and easterlies and northeasterlies in the mid- and upper troposphere. A brief analysis (not shown) reveals that the 850-hPa westerlies range between 3 and 5 m s^{-1} over the region west of 40°E, and exceed 15 m s^{-1} off the coast of Somalia. The 700-hPa mean northerlies range between 1 and 6 m s^{-1} over the region north of about 10°N. The 700-hPa positive relative vorticity ζ is dominant in the deep convective zone within 7.5°–12.5°N, including the southern Red Sea and western Arabian Sea, with average magnitudes ranging up to 3×10^{-5} s^{-1}. In the composite analysis below, low- to midtroposheric winds and ζ anomalies are to be interpreted in comparison with these average values.

Figure 9 displays regression composite anomalies of zonal (U850) and meridional winds (V700) and 700-hPa relative vorticity ζ'. The evolution of the three different
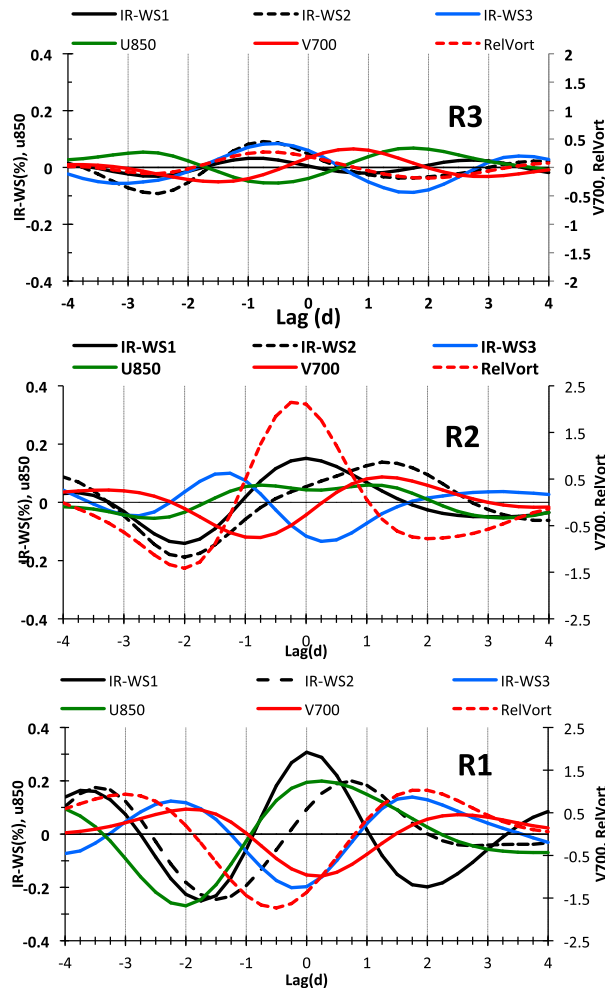
FIG. 9. The regression composite anomalies of IR-WS1, IR-WS2, IR-WS3, zonal (U850) and meridional (V700) winds (m s^{-1}), and relative vorticity (ζ'; s^{-1}; scaled by 10^{-6}) at 700 hPa. The ordinate on the right is for IR-WS and U850 and the one on the left is for meridional wind and ζ'. Regression composites are as in Fig. 7.

types of deep convection, IR-WS1, IR-WS2, and IR-WS3, is also presented.

(i) Region R3

The U850 anomalies are negative between day -2 and day $+0.5$, indicating weaker-than-average westerlies. As shown in Fig. 8, the region is characterized by low specific humidity, implying limited moisture availability in the lower levels of the troposphere. The ζ', IR-WS2, and IR-WS3 anomalies peak at or around the same time near day -0.5 but these are weak. Northerly anomalies precede deep convection.

(ii) Region R2

Positive ζ' peak at about the same time as maximum IR-WS1. Positive U850 anomalies (stronger than average)

precede maximum IR-WS1. Maximum northerly anomalies precede maximum IR-WS1 by about 12–18 h. IR-WS3 anomalies peak at about day -1.5, preceding both maximum ζ' and maximum northerly anomalies, and weaken after that. The sequence over R2 suggests IR-WS3 → V700 → ζ', IR-WS1.

(iii) Region R1

The sequence of events observed over R2 appears to be different compared with that over R1. The ζ' is negative between day -2 and day -1; it then drops to a minimum at day -0.5 and peaks at day $+1.5$. Maximum IR-WS1 precedes maximum northerly anomalies by about 6 h, the wind perturbations lagging well-organized large-scale convection. This suggests that large-scale and well-organized deep convection influences wave disturbances. As described earlier, IR-WS1 is more frequent over R1 compared with R2. The sequence over R1 indicates IR-WS3 → IR-WS1 → V700 (AEW).

In summary, IR-WS3 anomalies increase over R3, while they weaken just to the west of the region. IR-WS1 anomalies increase over the Ethiopian highlands (R2) and eastern and central Sudan (R1). This suggests smaller-scale deep convection transitioning into well-organized convection, first, over the Ethiopian highlands, then deepening further over the lowlands of eastern and central Sudan. Although weak, northerly meridional wind anomalies peak before deep convection over R3 and R2. In contrast, peak IR-WS1 precedes maximum northerlies over R1. This suggests that initially weak wind perturbations may have facilitated the transition of isolated deep convection over the region east of the Ethiopian highlands, but after the switching, convection grows deeper downstream and the enhanced convection coincides with maximum northerly anomalies. We expect that maximum upward ascent to coincide with maximum IR-WS1 development in association with peak northerlies or around the wave trough region, consistent with suggestions in Janiga and Thorncroft (2016). Also, over R1, deep convective clouds propagate westward slightly faster than the wave trough (as demonstrated by meridional winds; e.g., MR11). This suggests that the dominant sequence of events is IR-WS3 → IR-WS1 → AEW.

A Hovmöller analysis (not shown) of mean meridional winds and IR-WSs suggests that IR-WS3 transitions to IR-WS1 over the Ethiopian highlands and almost at the same time peak meridional winds appear, consistent with earlier findings that AEW perturbations are forced in association with well-organized and large-scale convection. Peak positive relative vorticity anomaly is observed over the Ethiopian highlands, but is much weaker to the west of the Ethiopian highlands. A maximum vorticity anomaly could
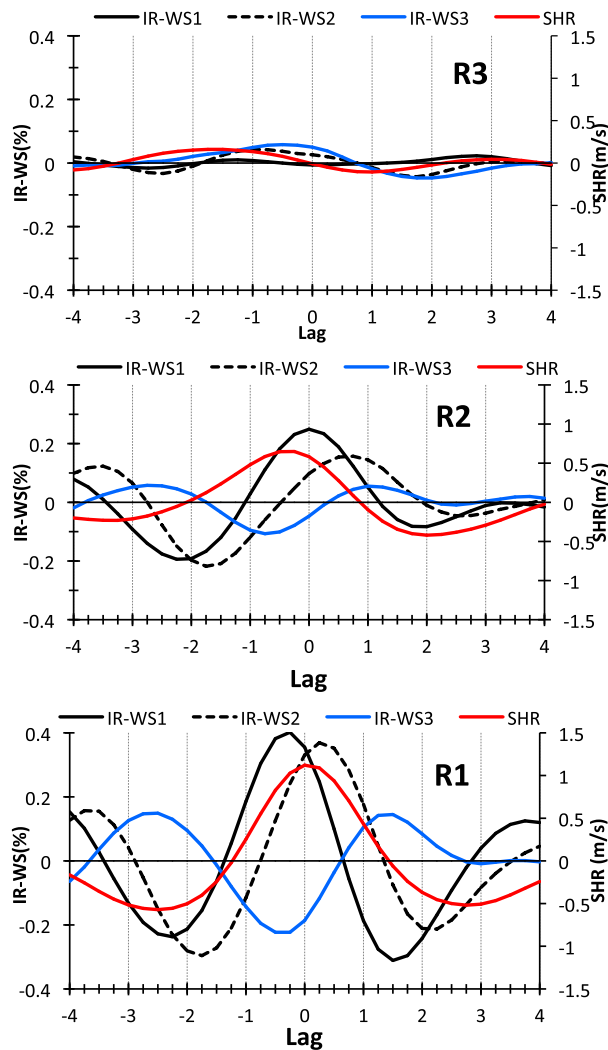
FIG. 10. The regression anomalies of IR-WS and 600–850-hPa vertical wind shear (SHR) based on 2–10-day filtered 600–850-hPa wind shear at 12.5°N, 32.5°E. The ordinate on the left shows the IR-WS anomalies. The ordinate on the right show shear anomalies. Lag times are every 0.25 day (6 h).

be viewed as a signature of wave initiation. In contrast, increasing vorticity could also be associated with the IR-WS1 type of convection initiated over the mountains, rather than an indication of wave vorticity. The results here indicate the latter because it appears to weaken downstream. Generally, increased vorticity over the mountains appears to favor the convection switching described above.

The transition from IR-WS3 to IR-WS1 is also favored by increased moist low-level westerlies (cf. Fig. 8). The environment for further convective development was favorable as suggested by an increase in θ_E and the positive specific humidity anomaly preceding maximum IR-WS1 over the Ethiopian highlands. This suggests that smaller and scattered cloud regimes cannot "keep up"

with the increasing instability and moistening, and grow into IR-WS1. Therefore, both the thermodynamic and dynamic environments favor the sequence IR-WS3 → IR-WS1 → AEW in East Africa.

2) THE IMPACT OF 600–850-HPA VERTICAL WIND SHEAR

As reviewed in sections 1 and 3, one of the important mechanisms for convective organization is moderate vertical wind shear. As shown in Fig. 6, the 600–850-hPa shear direction is dominantly northeasterly and easterly over tropical North Africa, a favorable environment for deep convection (e.g., Laing et al. 2008). Here, we examine the role of low- to midlevel shear magnitude on WS transitions. We construct a 2–10-day-filtered 600–850-hPa wind shear time series at base point 12.5°N, 32.5°E. Figure 10 shows composites of IR-WS1, IR-WS2, and IR-WS3 anomalies and 600–850-hPa wind shear; all projected onto to the shear time series.

(i) Region R3

The weather state and vertical shear anomaly amplitudes in this region are small, not significantly different from the climatology; but the absolute shear magnitudes over R3 are large (Fig. 6). Although small, the shear anomaly precedes positive IR-WS3 by about a day and the IR-WS3 anomaly is slightly higher than its mean frequency near day −0.5. In particular, IR-WS1's fluctuation is nearly zero, implying no significant influence of the low- to midlevel shear on IR-WS1. Results suggest that the low- to midlevel shear favors scattered and less well-organized clouds in the region.

(ii) Region R2

The IR-WS1 peaks at day 0, about half a day after a positive maximum shear amplitude, indicating a positive correlation between the occurrence of moderate shear and well-organized deep convection. Maximum IR-WS2 occurs at day +0.5, following IR-WS1. It is seen that the IR-WS3 amplitudes are small in this region with a minimum at day −0.5 and slightly positive at day +1. The shear fluctuation is out of phase with IR-WS3. The shear fluctuations over R2 are larger than over R3. The evidence suggests that a moderate increase in shear over R2 is in phase with increasing IR-WS1.

(iii) Region R1

The weather state amplitudes are almost twice as large in this region compared with R2. Maximum IR-WS1 occurs slightly earlier, at day −0.25, than the maximum shear anomaly. The fact that maximum IR-WS1 occurs at essentially the same time over R1 and R2 indicates that well-organized convection occupies a large area between

the Ethiopian mountains and eastern Sudan. The IR-WS2 peaks about half a day after IR-WS1 maximum. Shear anomalies and IR-WS3 anomalies are again out of phase.

Investigation of the interaction between low- to midlevel shear and different IR-WSs suggests that IR-WS1 forms in the increasing shear over R2, while shear interaction with IR-WS3 does not appear to be significant. The contrasting view that vertical wind shear can be a consequence of increasing deep convection is not evident in these results. The IR-WS1 and shear anomalies show switching from negative minimum to positive maximum in about a 2–3-day time scale, typical of synoptic-scale convection. Similar time-scale variability in organized convection (IR-WS1) is also consistent with the findings in Mekonnen and Thorncroft (2016). Results show that the vertical shear anomaly amplitudes are between -1.5 and $1.5 \, \mathrm{m \, s^{-1}}$, indicating a moderate increase or decrease compared with climatological values. Past work (e.g., Mohr and Thorncroft 2006; Laing et al. 2011, and references therein) suggest that moderate low-level shear, in tandem with large CAPE, is conducive for development and growth of deep convection. In summary, a slightly above-average (moderate) low-level shear magnitude is in phase with enhanced large-scale deep convection (i.e., IR-WS1) but out of phase with scattered and less well-organized convection (i.e., IR-WS3) over the Ethiopian highlands and the region to the west. The strong mean shear over the region to the east of the Ethiopian highlands favors the formation of IR-WS3 but not IR-WS1. Therefore, comparison of Fig. 10 with Figs. 8 and 9 suggests that a low- to midlevel shear contributes to the IR-WS3 → IR-WS1 sequence of events.

While a large-scale wind pattern of low-level convergence and high-level divergence may encourage more vigorous deep convection, the organization of the deep convection with an associated mesoscale circulation can alter this pattern. We briefly examined the relationship of the upper-level (200 hPa) wind convergence–divergence with the occurrence of IR-WS1 and IR-WS3. We found that the upper-level divergence strengthened just prior to the peak occurrence of IR-WS1, consistent with the large-scale winds being conducive to the formation of the mesoscale convective system. This also supports the IR-WS3 → IR-WS1 → AEW sequence of events.

5. Summary

The objective of this research was to investigate the process of weather state transitions and the associated major dynamic and thermodynamic mechanisms that determine the African easterly wave (AEW) initiation pathways; namely, IR-WS3 → IR-WS1 → AEW or IR-WS3 → AEW → IR-WS1.

Results based on 25 years of satellite and reanalysis datasets show that increasing intradiurnal activity, increasing atmospheric instability (as determined by increasing positive θ_E), and specific humidity precedes the development of well-organized and large-scale convection over the Ethiopian highlands. Atmospheric instability favors the higher frequency of a scattered, isolated-type convection (i.e., IR-WS3) to the east of the Ethiopian highlands. But this type of convection cannot "keep up" with the growing instability, so IR-WS3 is followed by a large increase in instability and increasing humidity over the Ethiopian highlands, which results in the formation of well-organized and larger-scale convection (i.e., IR-WS1). Thermodynamic processes suggest that the dominant process is IR-WS3 → IR-WS1 → AEW. Evidence show that high terrain associated with strong latent heating has an impact in transitioning of IR-WS3 to IR-WS1.

The θ_E and 700-hPa northerly wind anomalies peak at about the same time over the Ethiopian highlands (Figs. 8 and 9), indicating that increased instability favors the development of well-organized, larger-scale convection. Maximum relative vorticity (ζ') slightly precedes maximum convection over the Ethiopian highlands. Slightly before the IR-WS1 peaks over the mountains and to the west of the Ethiopian highlands, low-level moist westerlies, low- to midlevel increasing wind shear, and positive ζ' increase between central Sudan and Ethiopia. The AEW signatures over East Africa are weak during the time of convective transitioning. Results show that the large-scale and local environment including moderate increase in shear enables the IR-WS3 to merge and form larger and organized convective systems, IR-WS1, as they propagate westward and the IR-WS1 further develops over the region to the west of the Ethiopian highlands. Also, increased vorticity in association with increased moderate wind shear creates an environment favorable for the development of deep and well-organized convection. This leads us to conclude that the dominant pathway is IR-WS3 → IR-WS1 → AEW.

As discussed in Mekonnen and Rossow (2011), upper-tropospheric mean flow including upper-tropospheric wave disturbances enhance the IR-WS3 types over the Arabian Sea and southern Arabia and steers these clouds westward. As they move westward and interact with the mountains, they encounter additional lifting by the high terrain that aids the development of more vigorous and well-organized larger-scale clouds. The low-level vertical wind shear maximizes over the high

terrain, which enhances the further growth of MCS type activity. To summarize, dynamic and thermodynamic factors favor the development of IR-WS1 clouds and, as a response to the much stronger heating by the large-scale deep convection, easterly wave perturbations are forced over East Africa, then, AEW perturbations increase in strength westward in association with the AEJ environment over central and West Africa.

REFERENCES

Albignat, J. P., and R. J. Reed, 1980: The origin of African wave disturbances during Phase III of GATE. *Mon. Wea. Rev.*, **108**, 1827–1839, https://doi.org/10.1175/1520-0493(1980)108<1827:TOOAWD>2.0.CO;2.

Anber, U., S. Wang, and A. Sobel, 2014: Response of atmospheric convection to vertical wind shear: Cloud-system-resolving simulations with parameterized large-scale circulation. Part I: Specified radiative cooling. *J. Atmos. Sci.*, **71**, 2976–2993, https://doi.org/10.1175/JAS-D-13-0320.1.

Avila, L. A., and R. J. Pasch, 1992: Atlantic tropical systems of 1991. *Mon. Wea. Rev.*, **120**, 2688–2696, https://doi.org/10.1175/1520-0493(1992)120<2688:ATSO>2.0.CO;2.

Berry, G. J., and C. D. Thorncroft, 2005: Case study of an intense African easterly wave. *Mon. Wea. Rev.*, **133**, 752–766, https://doi.org/10.1175/MWR2884.1.

Burpee, R. W., 1972: The origin and structure of easterly waves in the lower troposphere of North Africa. *J. Atmos. Sci.*, **29**, 77–90, https://doi.org/10.1175/1520-0469(1972)029<0077:TOASOE>2.0.CO;2.

Carlson, T. N., 1969: Synoptic histories of three African disturbances that developed into Atlantic hurricanes. *Mon. Wea. Rev.*, **97**, 256–275, https://doi.org/10.1175/1520-0493(1969)097<0256:SHOTAD>2.3.CO;2.

Dee, D. P., and Coauthors, 2011: The ERA-Interim reanalysis: Configuration and performance of the data assimilation system. *Quart. J. Roy. Meteor. Soc.*, **137**, 553–597, https://doi.org/10.1002/qj.828.

Diaz, M., and A. Aiyyer, 2013: Genesis of African easterly waves by upstream development. *J. Atmos. Sci.*, **70**, 3492–3512, https://doi.org/10.1175/JAS-D-12-0342.1.

Diedhiou, A., S. Janicot, A. Viltard, P. de Felice, and H. Laurent, 1999: Easterly wave regimes and associated convection over West Africa and tropical Atlantic: Results from the NCEP/NCAR and ECMWF reanalyses. *Climate Dyn.*, **15**, 795–822, https://doi.org/10.1007/s003820050316.

Duchon, C. E., 1979: Lanczos filtering in one and two dimensions. *J. Appl. Meteor.*, **18**, 1016–1022, https://doi.org/10.1175/1520-0450(1979)018<1016:LFIOAT>2.0.CO;2.

Duvel, J. P., 1989: Convection over Tropical Africa and the Atlantic Ocean during northern summer. Part I: Interannual and diurnal variations. *Mon. Wea. Rev.*, **117**, 2782–2799, https://doi.org/10.1175/1520-0493(1989)117<2782:COTAAT>2.0.CO;2.

Fink, A. H., and A. Reiner, 2003: Spatio-temporal variability of the relation between African Easterly Waves and West African Squall Lines in 1998 and 1999. *J. Geophys. Res.*, **108**, 4332, https://doi.org/10.1029/2002JD002816.

Frank, N. L., 1970: Atlantic tropical storms of 1969. *Mon. Wea. Rev.*, **98**, 307–314, https://doi.org/10.1175/1520-0493(1970)098<0307:ATSO>2.3.CO;2.

Grabowski, W. W., and M. W. Moncrieff, 2004: Moisture-convection feedback in the tropics. *Quart. J. Roy. Meteor. Soc.*, **130**, 3081–3104, https://doi.org/10.1256/qj.03.135.

Hall, N. M. J., G. Kiladis, and C. Thorncroft, 2006: Three dimensional structure and dynamics of African easterly waves. Part II: Dynamical modes. *J. Atmos. Sci.*, **63**, 2231–2245, https://doi.org/10.1175/JAS3742.1.

Hodges, K. I., and C. D. Thorncroft, 1997: Distribution and statistics of African mesoscale convective weather systems based on the ISCCP Meteosat imagery. *Mon. Wea. Rev.*, **125**, 2821–2837, https://doi.org/10.1175/1520-0493(1997)125<2821:DASOAM>2.0.CO;2.

——, D. W. Chappell, G. J. Robinson, and G. Yang, 2000: An improved algorithm for generating global window brightness temperatures from multiple satellite infrared imagery. *J. Atmos. Oceanic Technol.*, **17**, 1296–1312, https://doi.org/10.1175/1520-0426(2000)017<1296:AIAFGG>2.0.CO;2.

Hsieh, J.-S., and K. H. Cook, 2005: Generation of African easterly wave disturbances: Relationship to the African easterly jet. *Mon. Wea. Rev.*, **133**, 1311–1327, https://doi.org/10.1175/MWR2916.1.

——, and ——, 2007: A study of the energetics of African easterly waves using a regional climate model. *J. Atmos. Sci.*, **64**, 421–440, https://doi.org/10.1175/JAS3851.1.

Huffman, G. J., and Coauthors, 2007: The TRMM Multisatellite Precipitation Analysis (TMPA): Quasi-global, multiyear, combined-sensor precipitation estimates at fine scales. *J. Hydrometeor.*, **8**, 38–55, https://doi.org/10.1175/JHM560.1.

Jakob, C., and G. Tselioudis, 2003: Objective identification of cloud regimes in the tropical western Pacific. *Geophys. Res. Lett.*, **30**, 2082, https://doi.org/10.1029/2003GL018367.

——, and C. Schumacher, 2008: Precipitation and latent heating characteristics of the major tropical western Pacific cloud regimes. *J. Climate*, **21**, 4348–4364, https://doi.org/10.1175/2008JCLI2122.1.

——, G. Tselioudis, and T. Hume, 2005: The radiative, cloud and thermodynamic properties of the major tropical western Pacific cloud regime. *J. Climate*, **18**, 1203–1215, https://doi.org/10.1175/JCLI3326.1.

Janiga, M. A., and C. D. Thorncroft, 2016: The influence of African easterly waves on convection over tropical Africa and the east Atlantic. *Mon. Wea. Rev.*, **144**, 171–192, https://doi.org/10.1175/MWR-D-14-00419.1.

Kiladis, G. N., C. D. Thorncroft, and N. G. Hall, 2006: Three-dimensional structure and dynamics of African easterly waves. Part I: Observations. *J. Atmos. Sci.*, **63**, 2212–2230, https://doi.org/10.1175/JAS3741.1.

Kummerow, C., and Coauthors, 2000: The status of the Tropical Rainfall Measuring Mission (TRMM) after two years in orbit. *J. Appl. Meteor.*, **39**, 1965–1982, https://doi.org/10.1175/1520-0450(2001)040<1965:TSOTTR>2.0.CO;2.

Laing, A. G., and J. M. Fritsch, 1993: Mesoscale convective complexes over the Indian monsoon region. *J. Climate*, **6**,

911–919, https://doi.org/10.1175/1520-0442(1993)006<0911:MCCOTI>2.0.CO;2.

——, R. Carbone, V. Levizzani, and J. Tuttle, 2008: The propagation and diurnal cycles of deep convection in northern tropical Africa. *Quart. J. Roy. Meteor. Soc.*, **134**, 93–109, https://doi.org/10.1002/qj.194.

——, R. E. Carbone, and V. Levizzani, 2011: Cycles and propagation of deep convection over equatorial Africa. *Mon. Wea. Rev.*, **139**, 2832–2853, https://doi.org/10.1175/2011MWR3500.1.

Lee, D., L. Oreopoulos, G. J Huffman, W. B. Rossow, and I.-S. Kang, 2003: The precipitation characteristics of ISCCP tropical weather states. *J. Climate*, **26**, 772–788, https://doi.org/10.1175/JCLI-D-11-00718.1.

Lin, Y. L., K. E. Robertson, and C. M. Hill, 2005: Origin and propagation of a disturbance associated with an African easterly wave as a precursor of Hurricane Alberto (2000). *Mon. Wea. Rev.*, **133**, 3276–3298, https://doi.org/10.1175/MWR3035.1.

Mathon, V., and H. Lauren, 2001: Life cycle of Sahelian mesoscale convective cloud systems. *Quart. J. Roy. Meteor. Soc.*, **127**, 377–406, https://doi.org/10.1002/qj.49712757208.

Mekonnen, A., and W. B. Rossow, 2011: The interaction between deep convection and easterly waves over tropical North Africa: A weather state perspective. *J. Climate*, **24**, 4276–4294, https://doi.org/10.1175/2011JCLI3900.1.

——, and C. D. Thorncroft, 2016: On the mechanisms that determine synoptic timescale convection over East Africa. *Int. J. Climatol.*, **36**, 4045–4057, https://doi.org/10.1002/joc.4614.

——, ——, and A. Aiyyer, 2006: Analysis of convection and its association with African easterly waves. *J. Climate*, **19**, 5405–5421, https://doi.org/10.1175/JCLI3920.1.

Mohr, K. I., and C. D. Thorncroft, 2006: Intense convective systems in West Africa and their relationship to the African easterly jet. *Quart. J. Roy. Meteor. Soc.*, **132**, 163–176, https://doi.org/10.1256/qj.05.55.

Moncrieff, M. W., 1981: A theory of organized steady convection and its transport properties. *Quart. J. Roy. Meteor. Soc.*, **107**, 29–50, https://doi.org/10.1002/qj.49710745103.

Nicholson, S. E., 2018: The ITCZ and the seasonal cycle over equatorial Africa. *Bull. Amer. Meteor. Soc.*, **99**, 337–348, https://doi.org/10.1175/BAMS-D-16-0287.1.

Norquist, C. D., E. E. Recker, and R. J. Reed, 1977: The energetics of African wave disturbances as observed during Phase III of GATE. *Mon. Wea. Rev.*, **105**, 334–342, https://doi.org/10.1175/1520-0493(1977)105<0334:TEOAWD>2.0.CO;2.

Oreopoulos, L., and W. B. Rossow, 2011: The cloud radiative effect of ISCCP weather states. *J. Geophys. Res.*, **116**, D12202, https://doi.org/10.1029/2010JD015472.

Parker, D. J., and Coauthors, 2005: The diurnal cycle of the West African monsoon circulation. *Quart. J. Roy. Meteor. Soc.*, **131**, 2839–2860, https://doi.org/10.1256/qj.04.52.

Reed, R. J., D. C. Norquist, and E. E. Recker, 1977: The structure and properties of African wave disturbances as observed during phase III of GATE. *Mon. Wea. Rev.*, **105**, 317–333, https://doi.org/10.1175/1520-0493(1977)105<0317:TSAPOA>2.0.CO;2.

Riehl, H., 1954: *Tropical Meteorology*. McGraw Hill, 392 pp.

Rossow, W. B., and R. A. Schiffer, 1991: ISCCP cloud data products. *Bull. Amer. Meteor. Soc.*, **72**, 2–20, https://doi.org/10.1175/1520-0477(1991)072<0002:ICDP>2.0.CO;2.

——, and ——, 1999: Advances in understanding clouds from ISCCP. *Bull. Amer. Meteor. Soc.*, **80**, 2261–2287, https://doi.org/10.1175/1520-0477(1999)080<2261:AIUCFI>2.0.CO;2.

——, G. Tselioudis, A. Polak, and C. Jakob, 2005: Tropical climate described as a distribution of weather states indicated by distinct mesoscale cloud property mixtures. *Geophys. Res. Lett.*, **32**, L21812, https://doi.org/10.1029/2005GL024584.

——, A. Mekonnen, C. Pearl, and W. Goncalves, 2013: Tropical precipitation extremes. *J. Climate*, **26**, 1457–1466, https://doi.org/10.1175/JCLI-D-11-00725.1.

Russell, J. O., A. Aiyyer, J. D. White, and W. Hannah, 2017: Revisiting the connection between African Easterly Waves and Atlantic tropical cyclogenesis. *Geophys. Res. Lett.*, **44**, 587–595, https://doi.org/10.1002/2016GL071236.

Segele, Z. T., and P. J. Lamb, 2005: Characterization of variability of Kiremt rainy season over Ethiopia. *Meteor. Atmos. Phys.*, **89**, 153–180, https://doi.org/10.1007/s00703-005-0127-x.

Semunegus, H., A. Mekonnen, and C. J. Schreck, 2017: Characterization of convective systems and their association with African easterly waves. *Int. J. Climatol.*, **37**, 4486–4492, https://doi.org/10.1002/joc.5085.

Simmons, A., S. Uppala, D. Dee, and S. Kobayashi, 2007: ERA-Interim: New ECMWF reanalysis products from 1989 onwards. *ECMWF Newsletter*, No. 110, ECMWF, Reading, United Kingdom, 26–35.

Simpson, R. H., N. Frank, D. Shideler, and H. M. Johnson, 1968: Atlantic tropical disturbances, 1967. *Mon. Wea. Rev.*, **96**, 251–261, https://doi.org/10.1175/1520-0493(1968)096<0251:ATD>2.0.CO;2.

Tan, J., C. Jakob, and T. P. Lane, 2013: On the identification of the large-scale properties of tropical convection using cloud regimes. *J. Climate*, **26**, 6618–6632, https://doi.org/10.1175/JCLI-D-12-00624.1.

Thorncroft, C., and B. Hoskins, 1994: An idealized study of African easterly waves. I: A linear view. *Quart. J. Roy. Meteor. Soc.*, **120**, 953–982, https://doi.org/10.1002/qj.49712051809.

——, and K. Hodges, 2001: African easterly wave variability and its relationship to Atlantic tropical cyclone activity. *J. Climate*, **14**, 1166–1179, https://doi.org/10.1175/1520-0442(2001)014<1166:AEWVAI>2.0.CO;2.

——, N. M. J. Hall, and G. N. Kiladis, 2008: Three-dimensional structure and dynamics of African easterly waves. Part III: Genesis. *J. Atmos. Sci.*, **65**, 3596–3607, https://doi.org/10.1175/2008JAS2575.1.

Tompkins, A. M., A. Diongue, D. J. Parker, and C. D. Thorncroft, 2005: The African easterly jet in the ECMWF integrated forecast system: 4DVar analysis. *Quart. J. Roy. Meteor. Soc.*, **131**, 2861–2885, https://doi.org/10.1256/qj.04.136.

Tromeur, E., and W. B. Rossow, 2010: Interaction of tropical deep convection with the large-scale circulation in MJO. *J. Climate*, **23**, 1837–1853, https://doi.org/10.1175/2009JCLI3240.1.

Tselioudis, G., W. Rossow, Y. Zhang, and D. Konsta, 2013: Global weather states and their properties from passive and active satellite cloud retrievals. *J. Climate*, **26**, 7734–7746, https://doi.org/10.1175/JCLI-D-13-00024.1.

Ventrice, M. J., and C. D. Thorncroft, 2013: The role of convectively coupled atmospheric Kelvin waves on African easterly wave activity. *Mon. Wea. Rev.*, **141**, 1910–1924, https://doi.org/10.1175/MWR-D-12-00147.1.

Viste, E., and A. Sorteberg, 2013: Moisture transport into the Ethiopian highlands. *Int. J. Climatol.*, **33**, 249–263, https://doi.org/10.1002/joc.3409.

Wheeler, M., G. N. Kiladis, and P. J. Webster, 2000: Large-scale dynamical fields associated with convectively coupled equatorial waves. *J. Atmos. Sci.*, **57**, 613–640, https://doi.org/10.1175/1520-0469(2000)057<0613:LSDFAW>2.0.CO;2.

Yang, G., and J. Slingo, 2001: The diurnal cycle in the tropics. *Mon. Wea. Rev.*, **129**, 784–801, https://doi.org/10.1175/1520-0493(2001)129<0784:TDCITT>2.0.CO;2.